MetaLink: Extending Air-to-Water Wireless Communications Using Passive Bianisotropic Metasurfaces

John Nolan
University of California San Diego
La Jolla, CA, USA
jmnolan@ucsd.edu

Baicheng Chen
University of California San Diego
La Jolla, CA, USA
b3chen@ucsd.edu

Xinyu Zhang
University of California San Diego
La Jolla, CA, USA
xyzhang@ucsd.edu

Abstract

Reliable cross medium (e.g., air-water) communication using radio frequency (RF) has remained an open-problem for decades. Currently, underwater devices cannot communicate directly with land-based or airborne devices. Typical solutions are inadequate when communicating through the boundary due to cross-medium boundary reflection/refraction/attenuation effects. We present MetaLink, an RF wireless communication system that enables underwater radios to communicate with airborne ones using novel underwater antenna design and 3D printed bianisotropic metasurface. MetaLink leverages bianisotropic structures that can correct for the severe boundary reflections/refractions between the air/water mediums, opening up the air/water medium as a viable communication channel without the need for multiple types of signals. We further exploit the electromagnetic properties of water to drastically scale down MetaLink's meta-atom size, and improve communication range. To examine real world communications performance from water to air, we prototype MetaLink and measure in a 14 ft deep swimming pool. Moreover, we push the robustness, reliability, and performance of MetaLink to its limit under various real-world circumstances. Our experiments demonstrate that MetaLink can communicate through the water/air boundary with SNR improvements of more than 35dB using WiFi modulation at distances of 14 ft and reach a simulated maximum of 95 ft within water using commercially available equipment and measured data.

CCS Concepts

• **Hardware → Wireless integrated network sensors**; **Wireless devices**; **Sensor applications and deployments**; **Sensor devices and platforms**.

Keywords

Multi-medium communications, cross-medium communications, meta-materials, IoT, ultra-small meta-atom, underwater communications
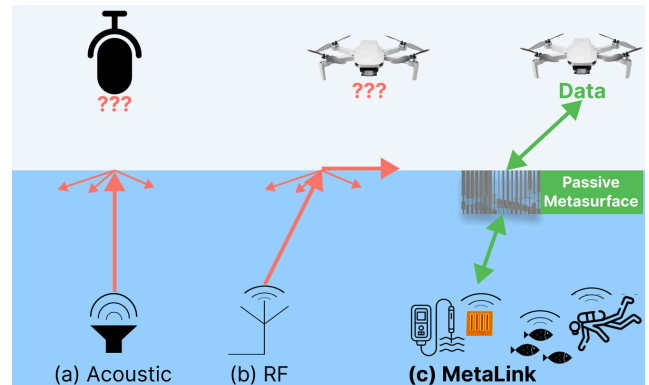
Figure 1: (a). Acoustic signals cannot penetrate the air-water boundary. (b). RF signals can penetrate the air-water boundary, but are heavily refracted to undesired directions. (c). MetaLink enables cross-medium communications by impedance matching and refracting signals in the desired directions.

1 Introduction

The underwater environment is crucial for research on aquatic health, exploration, and climate change, attracting significant interest globally [94]. The demand for advanced technologies is driven by global efforts and cooperation, with the underwater communications market projected to reach $7.2 billion by 2030 [106]. However, the asymmetric wireless channel between air and water hinders communication and sensing technologies. Applications like subsea networks [45], diver communication [26], and freshwater monitoring [16, 71] could greatly benefit from seamless communication across both mediums. Cross-media communication can also enable seamless integration of aerial and aquatic vehicles for comprehensive data collection and surveillance operations.

Current underwater communication systems rely on acoustics [24]. Acoustic systems are essential in highly conductive marine environments because RF systems experience significant attenuation. Unfortunately, acoustic systems rely on ultra-low-data-rate technologies which require expensive buoys to translate acoustic signals in water to RF for air communication [11]. In addition, the underwater acoustic link suffers from increased multi-path and severe noise pollution [22, 112]. Freshwater environments however, do not require acoustic technologies and can actually be unnecessarily limiting. RF systems can function effectively in freshwater, enabling seamless communication between air and water nodes with high data rates and low latencies. Bridging these two mediums presents

Modality/System	Cross-medium Problem/Solution	Data rate	Latency	Distance	Impact factors
Acoustic	✕	bps	High	Long	Air/Depth/Temp
Magnetic	✓	Mbps	Low	Short	Depth/Temp
Optic	Scattering+Refraction at boundary	Mbps	High	Medium	Surface wave/Alignment
RF	Reflection+Refraction at boundary	✕	Low	Short	Depth/Conductivity
TARF [99]	Acoustic UW + mmWave air	400 bps	High UW	1.3m UW	Alignment/1-Directional
AmphiLight [18]	Ultrasound + Laser	5.04 Mbps	Low	6.1m UW	Surface wave/Depth/Temperature
Zygo [117]	Reflection+Refraction at boundary	< 2 Mbps	Low	<0.67m UW	Depth
MetaLink	**Passive metasurface**	**65 Mbps**	**Low**	**4.3m UW**	Conductivity

Table 1: MetaLink advantage over modalities and state of the art systems, UW: under water

unique challenges stemming from their distinct electromagnetic (EM) properties [49, 64, 97]. As illustrated in Fig.1(a), underwater acoustic waves cannot penetrate the air-water boundary due to impedance differences, resulting in severe reflections [48]. Exiting water, acoustic energy decays rapidly in air, limiting range. RF signals (Fig.1(b)) also face reflection and refraction challenges at the air-water boundary, constraining the field of view (FoV) for cross-medium communication [51].

Alternative signaling methods, *i.e.,* optical and magnetic, have their own limitations [64]. Optical systems impose impractical alignment requirements between directional transceivers [18]; while magnetic solutions suffer from low data rate (e.g., < 1 Mbps) and trade off with communication distance (e.g., 10s of meters) [39, 63]. *Simply put, underwater nodes cannot communicate effectively with airborne nodes.*

In this paper, we present MetaLink, a novel RF cross-medium communication/sensing solution, which introduces a bianisotropic metasurface to break the air/water boundary bottleneck. As shown in Fig.1(c), the MetaLink metasurface allows *RF signals to penetrate the air-water boundary from both directions without reflections and refraction issues* while simultaneously improving the FoV from water to air. The bianisotropic property of the MetaLink metasurface allows for impedance matching [8] between highly dissimilar EM properties and for corrections due to refraction. The bianisotropic metasurface consists of deeply sub-wavelength meta-atoms (*i.e.,* < $0.03\lambda_o$, λ_o is the wavelength in air which is the smallest at the time of writing) which are composed of dielectric layers made with polylactic acid (PLA), a common 3D printing material. This design takes advantage of rapid prototyping and cost-effective fabrication, facilitating mass implementation.

Furthermore, MetaLink maintains the superior latency of RF communication, as EM waves naturally propagate approximately 22,000 times faster than sound in water. MetaLink ushers in a new era for cross-medium communication and applications. Table 1 summarizes the advantages of MetaLink compared to state-of-the-art underwater or water-air communication systems.

To craft MetaLink, we note that uplink and downlink channels require RF signals to propagate through water and air mediums, which demands a new asymmetric communication system design. The specific challenges include:

(i) The MetaLink communication system requires functional underwater antenna (UWA) designs that can operate in a non-static medium [53]. Water's EM properties vary with frequency, salinity, and temperature. The antenna design needs to be resilient against such variations in order to maintain a stable communication link.

(ii) Similarly, the non-static water medium poses challenges on the metasurface design. Specifically, high dielectric losses due to the molecular dynamics of water requires the use of lower frequencies, which poses a problem for practical metasurface designs whose form-factor grows inversely with frequency.

(iii) Lastly, the uniquely asymmetric channel creates challenges when adapting modulation schemes or adjusting center frequencies due to the time varying nature of the air-water cross medium channel. Although channel estimation could be fed back to both receivers since the MetaLink channel is bidirectional, the initial establishment of the communication link could be hampered without prior environmental knowledge.

To overcome these challenges, MetaLink consolidates the following design components:

(i) MetaLink creates a truly UWA phased array composed of substrate-windowed antenna elements connected using strip-line transmission lines which, to our knowledge, is a first of its kind for underwater applications at UHF frequencies. Strip-line transmission lines are impervious to the varying water properties since they are electrically isolated from the environment.

(ii) MetaLink leverages the high index of refraction of water at low frequencies to design an all-dielectric meta-atom with many degrees of freedom (DoFs) that is also deeply sub-wavelength. Each metaatom consists of a mix of water and PLA, with dimensions $0.03\lambda_o \times 0.03\lambda_o \times 0.3\lambda_o$ which to our knowledge, is the smallest of its kind.

(iii) Adapting the carrier frequency to varying EM properties underwater. We show that the air-water asymmetric channel is highly multipath-rich, resulting in severe frequency selectivity. By utilizing a temperature sensor within the water environment, an aquatic node can determine the optimal frequency of operation which minimizes channel losses. MetaLink UWA is designed to be broadband and directive enough to withstand temperature changes. In our experiments we show that MetaLink can work in 15.5 to 26.5°C, common daily temperature fluctuations. We designed and fabri-
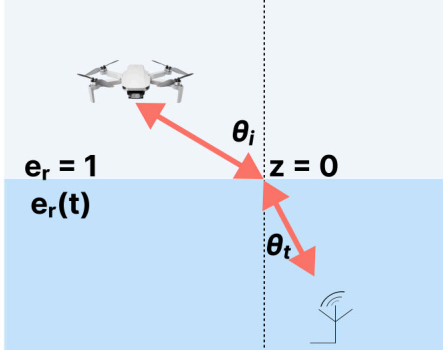
Figure 2: Air/Water boundary refraction model

Figure 3: Asymmetrical air/water vs. water/air refraction

cated METALINK hardware components using traditional printed circuit board (PCB) and 3D printing techniques. We experimentally verified the METALINK system in an outdoor swimming pool with practicing swimmers present. Our results indicate that:

- METALINK can refract EM signals from +/-30°, providing a 5× improvement in the FoV when crossing the air-water medium.
- METALINK can achieve a simulated SNR of higher than 20 dB through 29m of water, translating to data-rates of 65Mbps [2, 61, 77, 86, 88, 98] using a single spatial stream following the standard WiFi modulation and a measured SNR of 35 dB through 4.3m of water.
- METALINK is robust in the presence of large water surface waves and throughout the daily fluctuations of temperature.

To our knowledge, METALINK is the first end-to-end system using bianisotropic metasurfaces for air-water cross boundary communication/sensing at radio frequencies. We present the UWA design for UW nodes, fabricate a metasurface for various implementations, and evaluate this technology using commercial-off-the-shelf equipment. We also demonstrate that it can achieve standard WiFi data rates in water/air scenarios where previous technologies fall short.

2 Related Work

METALINK expands on previous work in three main fields, UWA design, cross-medium communications, and metasurfaces. METALINK differentiates itself from past work by designing and validating a complete and practical end-to-end RF communication system that can communicate through the air-water boundary.

Underwater Communications and Antenna Design Early systems utilized acoustic and ultrasonic transceivers for submarine-to-submarine communications and SONAR [12]. Today, interest in acoustic systems has surged due to the oil and gas industry and ocean exploration. However, initial acoustic systems faced challenges breaching the water-air boundary, leaving sub-sea networks isolated [99]. Acoustic technologies offer limited data rates, typically around 100 bits-per-second (bps). Commercial solutions [23, 26] allow divers to send preprogrammed acoustic messages up to 100 meters underwater. Although RF underwater communication was once deemed impractical, theoretical analysis has demonstrated its viability for multi-meter range [85]. Yet, current RF antenna designs suffer from size constraints or insufficient bandwidth [1, 29, 50]. Previous UWAs operated at frequencies in the
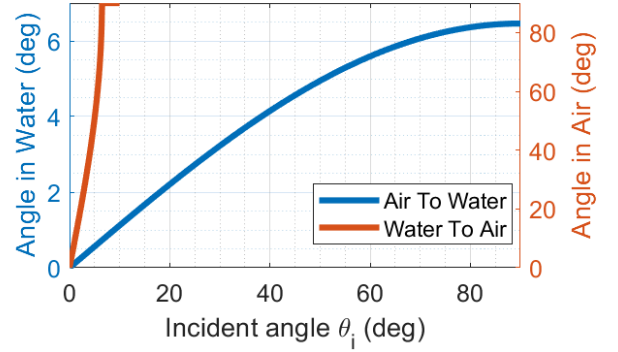
tens of MHz, constraining practical bandwidth and size. An ultra-wideband antenna (UWB) designed for 1.3-7.2 GHz [3, 95] offers ample bandwidth, but its frequency range poses challenges for underwater applications due to extreme path loss. METALINK has been designed to minimize dielectric losses from propagating in water by judicious selection of operating frequencies. The frequency selection is then used to design and optimize METALINK underwater antenna and bianisotropic metasurface. METALINK's UWA is truly designed for water unlike previous designs which design an air antenna and measure the performance in water [92].

Cross-Medium Technologies. Metasurfaces have been proposed to improve cross-medium sensing. In [67], a metasurface was used to enhance the penetration depth of 5 GHz WiFi signals in building walls to improve coverage. Similarly, in [41], radar is used for pipe detection in concrete blocks. In both works, the EM properties of the material are not as extreme as between air and water. In addition, wave-front control for arbitrary refraction is not included, limiting their applications for water-to-airborne links. In [107], a metallic 2.4 GHz metasurface was designed for anti-reflection and wavefront manipulation. Using metal PCB designs, limits the number of DoFs that can be easily added compared to 3D-printable ones such as METALINK. In addition, the unit cell size is insufficient to meet the air/water boundary requirements. Lastly, metallic solutions are not viable for submerging in water and requiring proper isolation from the water environment. Commercial solutions such as [117] use the ISM band to create a push-to-talk solution for swimmers. A special transceiver converts Bluetooth signals to a lower frequency for water propagation. However, the communication range is limited to 1-2 ft underwater. Lastly, [32, 99] designed a novel acoustic/mmWave system to communicate through the air/water boundary using radar. However, the underwater segment still relies on narrowband and low-rate acoustic signals, and data can only flow unidirectionally from the water into the air.

Metasurface Design. Metasurfaces can enhance EM wavefront control, leading to exotic physical phenomena which transcends the abilities of natural materials [46, 54]. Use cases of metasurfaces range from sensing, imaging, communications, *etc.* [90, 100].

In [82], small V shape rods etched onto a dielectric substrate are used for enhanced optical imaging. Imaging applications have leveraged metasurfaces to improve resolution by harnessing the information embedded in evanescent waves which are bound to the object [19, 62]. In addition, all-dielectric metasurfaces gained traction in imaging applications because they are less lossy than
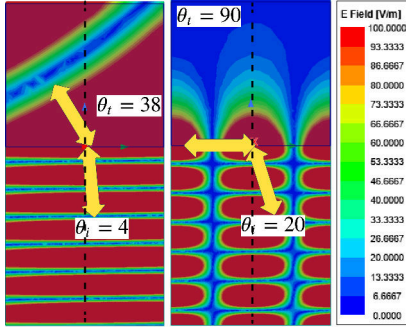
Figure 4: Snell's law refraction simulation

their metallic counterparts [14, 47, 58, 65, 70, 74, 101, 109, 110].

Aside from imaging, metasurfaces have also been used in cross-medium applications for acoustics. For example, in [15, 114], multiple acoustic metasurfaces are used to enhance transmission between water and air with 30% efficiency. In [20, 30, 44], multi-layer metasurfaces were used to reduce reflections at the boundary between media with permittivities in the range of 4-35. METALINK achieves cross-medium operation at a permittivity of 79 which poses significant meta-atom design challenges. METALINK meta-atoms are ultra-small and can simultaneously achieve impedance matching and phase shifting from both incident directions. Furthermore, METALINK meta-atoms are 3D printable which translates to lower costs. Lastly, the meta-atom design follows a closed form solution which makes for a straightforward design and simulation procedure unlike metallic solutions which require significant fine-tuning [107] and optimization.

3 Understanding the Asymmetric Air/Water Channel

The METALINK air-water channel consists of three components which affect RF wireless signal propagation: the air channel, the underwater channel and the interface between the two mediums. In this section, we will present the asymmetric channel dynamics that occur between dissimilar media, define a FoV metric and determine the optimal frequency of operation.

3.1 How do signals propagate through two mediums?

RF signals propagating within and between dissimilar media have been studied extensively and are well documented. EM signals propagating between differing mediums follow the well known *Snells' law* [102] which dictates how the signals will reflect and refract:

$$n_i sin(\theta_i) = n_t sin(\theta_t) \tag{1}$$

Following the boundary diagram shown in Fig.2, the air medium above (*i.e.,* $z < 0$) has a refractive index of $n_{air} = \sqrt{e_r \mu_r} = 1$ and the water medium below (*i.e.,* $z \geq 0$) has a refractive index of $n_{water}(t) = \sqrt{e_r(t)\mu_r}$, which varies over time due to the varying EM properties of water [36]. At low frequencies and at room temperature, the index of refraction of water is roughly $n_{water} \approx \sqrt{79} \approx 9$ [53]. Incident EM signals propagating in direction θ_i will refract to a new direction θ_t within the second medium following Eq.(1). Given that EM signals will refract differently depending on whether the incident signals
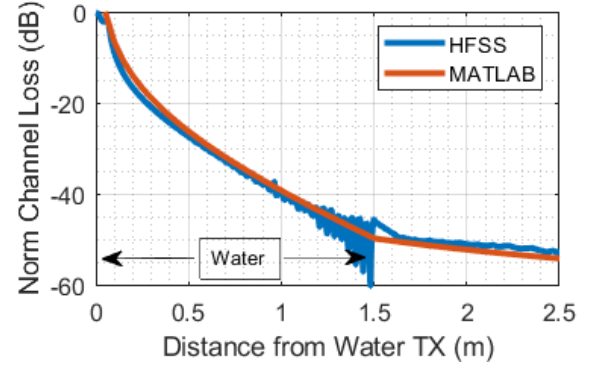

Figure 5: Water to air channel loss

originate in air or water (*i.e., asymmetric*), an FoV metric can be defined. This FoV metric expresses the maximum range of angles that sensor nodes can launch EM signals towards the air/water boundary. As shown in Fig.3, incident EM waves in air can penetrate the water boundary from all angles (*i.e.,* 0-90°). However, when refracted into water they will appear as if the signals came almost from directly above, since the range of possible refracted angles are 0-6.5°. Going in the other direction, *incident waves in water cannot penetrate the air/boundary from all angles* and are limited to $\theta_i = 0 - 6.5°$.

Beyond these angles, known as the *forbidden region* [44], *evanescent waves are produced which experience exponential decay as they penetrate the water-air interface and propagate into the air medium. Therefore, the RF channel across the air-water mediums has a maximum FoV of* $\approx 2 \times 6.5° = 13°$.

In addition to determining the FoV, understanding the channel loss mechanisms between the two mediums is necessary for fully analyzing the asymmetric channel. Back-of-the-envelope formulas for attenuation such as $0.0173\sqrt{f\sigma}$ [17] do not directly apply at all frequencies. As is well known, optical frequencies are minimally attenuated in water environments which according to the formula, would not be true. Therefore, it is best to apply Maxwell's equations to the boundaries. For signals transmitted in air, the electric field can be defined as follows:

$$E(\omega, t) = \begin{cases} E_o e^{-j\vec{\beta}_i \cdot \vec{r}_i} e^{j\omega t} & z < 0 \\ E_o T e^{-\alpha_c} e^{-j\vec{\beta}_t \cdot \vec{r}_t} e^{j\omega t} & z \geq 0 \end{cases} \tag{2}$$

where $E_o, \beta, \vec{r}, \omega, t, T, \alpha_c$ are the initial electric field intensities, wave-number $\beta = \frac{2\pi\sqrt{e_r}}{\lambda}$, 2D unit vector in spherical coordinates $(0, y \sin\theta, z\cos\theta)$, frequency, time, transmission coefficient, and the attenuation constant due to conductive losses, respectively. The subscripts i and t represent the incident and transmitted mediums. The transmission coefficient T describes the loss due to the impedance mismatch between the two mediums, *i.e.,* $T = \frac{2\eta_i}{\eta_i + \eta_t}$ [27] where η is the impedance of the medium (*i.e.,* $\eta \approx \frac{120\pi}{\sqrt{er}}$). As the EM wave enters the water, the conductivity of the medium will attenuate the signal and is represented by the attenuation constant α_c as:

$$\alpha_c = \omega\sqrt{\mu\epsilon}\sqrt{\frac{1}{2}(\sqrt{1 + \tan(\delta)^2} - 1)}, \text{ where } \tan(\delta) = \frac{\omega\epsilon'' + \sigma}{\omega\epsilon'} \tag{3}$$

In Eq.(3), ϵ' and ϵ'' refer to the real and imaginary components of the permittivity written as $\epsilon = \epsilon_o(\epsilon_r + j\epsilon'')$. Essentially, $\tan(\delta)$
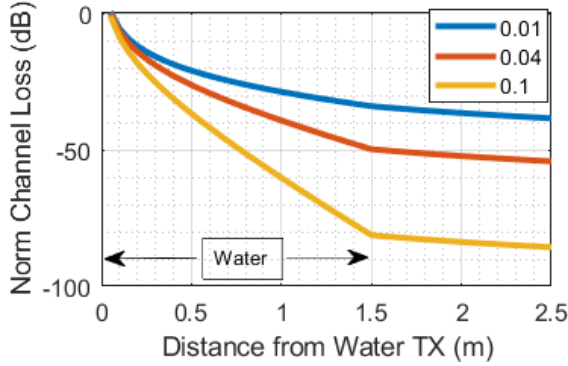
Figure 6: Water to air channel vs tan(δ)

Figure 7: Water Dielectric Loss vs Frequency and Temperature

accounts for all loss mechanisms, conductive (σ) and dielectric (ϵ'') [27], and is called the *loss tangent* of the medium. *Since the conductivity of the medium σ, cannot be changed, in order to minimize losses, we must minimize ϵ''.* In air, $\alpha_c = 0$, since air is non-conductive and has no imaginary component. This explains why RF signals are so efficient for wireless communications in air, whereas acoustic signals are not as they undergo exponential attenuation in air. On the other hand, for signals originating from the water and incident upon the water-air boundary, the electric field equations are different:

$$E(\omega, t) = \begin{cases} E_o T e^{-\alpha_e} e^{-j\vec{\beta}_t \cdot \vec{r}_t} e^{jwt} & z < 0 \\ E_o e^{-\alpha_c} e^{-j\vec{\beta}_t \cdot \vec{r}_t} e^{jwt} & z \geq 0 \end{cases} \quad (4)$$

where α_e = represents the attenuation due to refraction at forbidden angles dictated by Eq.(1). As shown in Fig.3, angles beyond the allowable region (*i.e.*, 6.5°) produce refracted angles of 90°, which propagate along the boundary (*i.e.,*, the water surface) and are attenuated heavily as they travel within air. The attenuation α_e can be calculated as follows:

$$\alpha_e = n_i \beta_o \sqrt{\sin^2 \theta_i - \sin^2 \theta_c} \text{ where, } \theta_c = \arcsin \frac{n_t}{n_i} \quad (5)$$

where θ_c is known as the critical angle which is the limit prior to the creation of an evanescent wave.

To demonstrate the impact of the limited FoV of the air/water channel, suppose an incident EM wave originates from the water medium at an angle of $\theta_i = 4°$. According to Eq.(1), the refracted angle will be $\theta_t = 38°$ assuming an index of refraction of 9.

As shown in the left figure of Fig.4, a plane wave propagating within water refracts heavily with a small incident angle. This is due to the large difference in refractive indices between water and air. Now suppose an incident EM wave in water propagates at an angle beyond the FoV, $\theta_i = 20°$. The refracted EM wave shows a highly distorted plane wave which is bound to the air/water interface with no electric field above the boundary, as illustrated in the right figure of Fig.4.

Now to determine the channel loss and the viable link distance that an end-to-end cross medium platform can achieve, we look at Eq.(2) and Eq.(4) to calculate the power versus distance for a given direction of EM signal propagation:

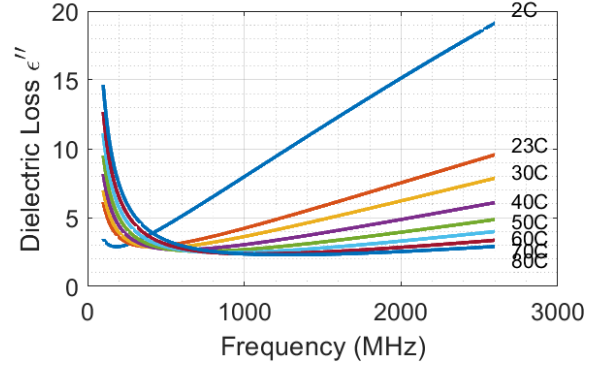$$P(r) = \frac{|E(\omega, t)|^2}{2\eta_o} \left(\frac{\lambda}{4\pi r}\right)^2 \quad (6)$$

As an example, using Eq.(6), we calculate the channel loss as a function of distance for a transmitter placed 1.5m in water pointing towards the air/water interface (*i.e.*, $\theta_i = 0$). The water loss tangent as described in Eq.(3), is set to $\tan(\delta) = 0.04$, which is a common value for fresh water systems [84]. The channel loss is plotted in Fig.5 using MATLAB and HFSS which is a 3D full-wave finite-element-method (FEM) based EM solver [4]. Using HFSS, confirms that the MATLAB model is accurate for METALINK design. The channel loss is exponential in water until the air-water boundary at 1.5m in which the loss starts to drop off slowly in air. The oscillations that appear in the HFSS results near 1.5m are due to the back-and-forth reflections that impedance discontinuities create at the boundary between dissimilar media. This phenomena is not accounted for in the channel model of Eq.(2) and Eq.(4). These phenomena contribute to the high multi-path and frequency selective fading that the air/water channel applies to communication systems.

The EM properties of water as depicted in Fig.2 vary with time. Specifically, the permittivity of the water medium varies with temperature, frequency and conductivity. *Since the channel model as described in Sec.3.1 heavily depends on the EM properties, which vary with time, we can say that the air/water channel is a linear-time-varying channel.* To cope with the time-varying property of the air/water channel, a temperature sensor can be used by the water node to directly calculate the optimal frequency of operation to minimize loss. In addition, an airborne node can leverage a temperature sensor to infer the water temperature from the air using a model similar to [115].

The temperature dependent permittivity of water can be described by an empirical formula as shown below [36]:

$$\epsilon'(T) = \epsilon_\infty + \frac{\epsilon_s - \epsilon_\infty}{1 + \omega^2 \tau^2} \quad (7)$$

$$\epsilon''(T) = \frac{(\epsilon_s - \epsilon_\infty)\omega\tau}{1 + \omega^2 \tau^2} + \frac{\sigma}{\omega\epsilon_o} \quad (8)$$

The variables, $\epsilon_\infty, \epsilon_s$, and τ were measured versus temperature and have empirical formulas as well. Due to space constraint, we refer the interested readers to [36] for more details. As $\epsilon'(T)$ varies with temperature, the impedance at the boundary will change which can be accounted for by careful METALINK design. On the other hand, $\epsilon''(T)$ will affect channel losses by increasing the $\tan(\delta)$ of the medium. Using the channel model we vary the loss tangent of the water medium, $\tan(\delta)$, between 0.01-0.1 and plot the channel loss. As shown in Fig.6, an additional 30dB of loss is incurred when
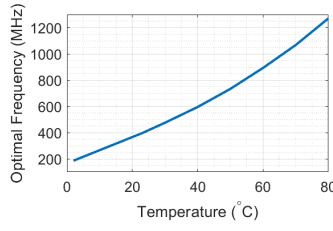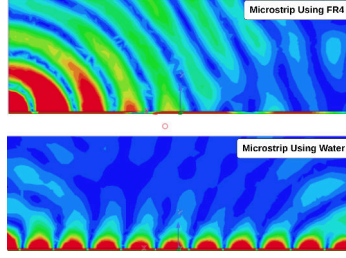
Figure 8: Optimal Frequency vs Temp.
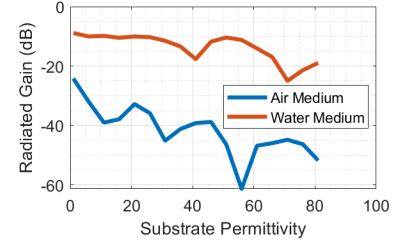

Figure 9: E Field above Microstrip.

Figure 10: Radiated emission gain.

$\tan(\delta)$ increases to 0.1. *Therefore, practical communication distances for water-to-airborne nodes can only be achieved by minimizing* $\tan(\delta)$.

To highlight the impact of temperature and frequency on the loss tangent, $\tan(\delta)$, we plot $\epsilon''(T)$ as shown in Fig.7. Minima can be seen versus frequency which can be leveraged for selecting an optimal frequency of operation. To minimize losses, we minimize $\epsilon''(T)$ by taking the first derivative w.r.t. frequency and set the value to 0:

$$\frac{d\epsilon''(T)}{d\omega} = \frac{1}{\sqrt{2}}\sqrt{\frac{-2B^2C}{AB^2 + B^4C} + \frac{A}{AB^2 + B^4C} - \frac{\sqrt{A}\sqrt{A - 8B^2C}}{AB^2 + B^4C}} = 0 \tag{9}$$

where $A = \epsilon_s - \epsilon_\infty$, $B = \tau$, and $C = \frac{\sigma}{\epsilon_o}$. Using Eq.(9), the optimal frequency vs. temperature can be found and is shown in Fig.8. The optimal frequency at room temperature, $23°C$ is found to be 396MHz. *Given that an ISM band exists at 433.92MHz in Region 1 [35], we adopt this frequency for* METALINK *which is close to the optimal value. Using this frequency of operation,* METALINK *maximizes range for air to water communications by reducing loss.*

4 METALINK Hardware Design

Having acknowledged the constraints posed by the air-water channel and the restricted FoV achievable between underwater and airborne nodes, our focus shifts to hardware strategies for addressing these challenges. The METALINK end-to-end system encompasses two main components: a novel UWA and an impedance matching metasurface. In the following section, we will delve into the details of the UWA design and elucidate the features of the metasurface. Both devices are designed to satisfy a minimum of 20MHz of RF bandwidth which is standard for common communication systems such as Wi-Fi [33].

4.1 Underwater Phased Array Design

Conventional RF antennas do not work underwater where medium properties differ from air, necessitating a new antenna design. Phased arrays use a collection of radiating elements to produce sharper beams and higher gain. Increasing the gain improves communication and sensing distances and mitigates multi-path. In the air-water channel scenario, having a high gain antenna helps in reducing the conductive losses due to the water medium. In the following sections, we describe the design details of METALINK's underwater, UHF band, phased array antenna.

4.1.1 Why don't microstrip transmission lines work underwater? Antenna arrays are typically designed by using transmission lines such as microstrip [43, 76] to connect multiple antenna elements that form an array. Microstrip lines consist of metal

traces with a specific width and length which defines its electrical impedance. Microstrip transmission lines are commonly used in antenna and RF circuits due to their ease of fabrication. However, a well known limitation is that microstrip leaks EM waves [28, 31, 89]. For most applications, the EM leakage is negligible. In the underwater environment however, the microstrip radiation is too significant for proper transmission line performance. We found that microstrip is not a viable option for UWA designs due to the large refractive index of water compared to that of common circuit board materials.

To quantify the underwater radiation characteristics of microstrip transmission lines, the total radiated power emanating from a microstrip can be computed as [42]:

$$P_r = \frac{I_o \eta (\beta^2 L h)^2}{3\pi}\left(1 + \frac{\epsilon_{eff}}{\epsilon_{sub}^2}\right) \tag{10}$$

The constants $I_o, h, \epsilon_{eff}, \epsilon_{sub}$ are the current, substrate height, effective permittivity of the microstrip transmission line, and the permittivity of the substrate. For details on the derivation, we refer the readers to [42]. The effective permittivity of the microstrip follows an empirical formula [76] defined as:

$$\epsilon_{eff} = \frac{\epsilon_{sub} + \epsilon_{medium}}{2} + \frac{|\epsilon_{sub} - \epsilon_{medium}|}{2}\left(1 + 12\frac{h}{w}\right)^{\frac{-1}{2}} \tag{11}$$

For microstrip transmission line designs for air applications, ϵ_{eff} is within, $1 < \epsilon_{eff} < \epsilon_{sub}$ since the permittivity of the medium is air (*i.e.,* $\epsilon_{medium} = 1$). In air applications, $\frac{\epsilon_{eff}}{\epsilon_{sub}^2} < 1$, which leads to minimal radiation. *However, in the underwater environment where* $\epsilon_{medium} \gg 1$, *the radiation factor can be much larger than 1, leading to excessive radiation power leakage.*

To verify the above result, we simulate a microstrip line in HFSS. The microstrip is designed to have a 50 Ohm impedance with a
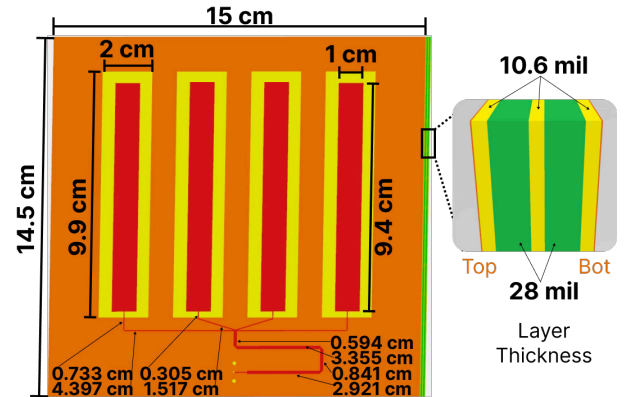

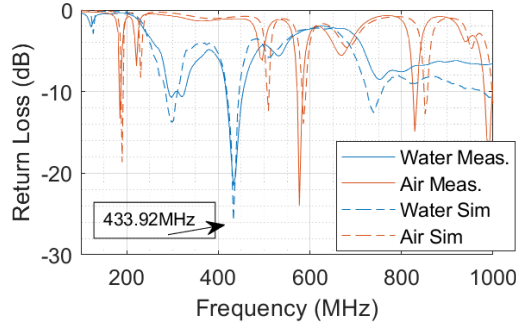Figure 11: UHF Phased Array Geometry Details.

Figure 12: UWA return loss

Figure 13: Return loss at 433.92 Mhz

width of 5.9mm, height 2.54mm, and is placed on a FR4 substrate material with a $\epsilon_{sub} = 4.4$. We assume the medium above the microstrip is water. As shown in the top figure of Fig.9, the electric fields are radiating away from the microstrip line and do not reach the other side, indicative of undesired radiation. The return loss (*i.e.,* S11) of this design is 13dB with an insertion loss of 18dB, which is not acceptable. To further validate Eq.(10), we perform a sweep of the substrate permittivity within air or water environments and calculate the gain of the leaky radiation. As shown in Fig.10, at low substrate permittivities, the water environment produces significant radiation compared to the air environment. As the substrate permittivity approaches that of water, the radiation leakage decreases as expected following Eq.(10).

Next, we verify the design using a water substrate such that $\epsilon_{sub} = 79$ to reduce radiation. In the bottom figure of Fig.9, we see that the E field lines are confined to the surface of the microstrip and show a wave traveling down the transmission line. This design has an S11 of 27dB and an insertion loss of 0.5dB which is acceptable for antenna array applications. However, the drawback is that the microstrip needs to be suspended in water which is impractical.

In contrast, strip-line designs have no radiation leakage since they are covered by metal. Strip-lines are formed by sandwiching a microstrip line between two metallic layers [76]. To verify the strip-line performance, we simulate a design using HFSS with two substrates, each 2.54mm thick, covered by metal and water above.

The return loss was found to be 52dB with an insertion loss of 0.1dB. *Given the above analysis and results, we adopt strip-line transmission lines to design the antenna array for underwater applications.*

4.1.2 ***How to design an underwater phased array?*** The patch antenna is designed using HFSS. The resonant frequency of the design is 433.92MHz as discussed in Sec.3.1. The substrate was chosen to be FR4 which is a common low frequency and low cost substrate for antenna designs [57] and is impervious to detiroration from water [40]. The PCB stack-up consists of two 0.7112mm FR4 cores and three 0.26924mm FR4 prepreg cores with dimensions shown in Fig.11. The top and bottom layers of the board are used as ground planes to create the strip-line transmission lines. The patch and strip-line designs are placed one layer below the top ground plane. Openings 9.9cm×2cm are made in the top ground layer to expose the patch antennas below to the water environment. The conventional design equations formulated for microstrip patch antenna geometries (*i.e.,* length and width) are not directly applicable to underwater environments. However, with slight modifications,
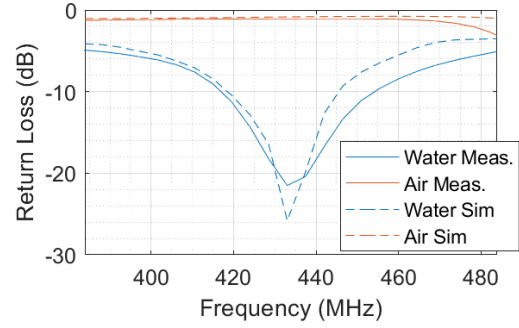
these equations serve as a starting point [27].

$$L = \frac{c}{2f_o\sqrt{\epsilon_{eff}}}, W = \frac{c}{2f_o\sqrt{\frac{\epsilon_{sub}+\epsilon_{medium}}{2}}} \qquad (12)$$

where ϵ_{eff} follows Eq.(11). The length and width of the patch antennas, after HFSS optimization, are 9.4×1cm. These dimensions achieve a return loss of 10dB or better at 433.92MHz. The patch dimensions are 20× and 2× smaller, respectively, in width and length than those of a design intended for use in air. Since strip-line was selected as the transmission line, the patch antenna is fed using edge-connected strip-lines. Other feeding techniques, such as proximity coupling, require ultra-high permittivity substrates to better match the impedance of the water environment and patch.

The patch antennas are connected using a 4-way combiner [38] which avoids the need for resistors like those used in Wilkinson power combiners [76]. The geometrical details are shown in Fig.11. The 4-way combiner is then connected to a through hole via which connects the surface mount SMA connector [96]. The completed antenna array design has a simulated gain of 13dB in water.

The UWA design was fabricated using conventional PCB techniques. The return loss was verified using a vector network analyzer [56] in air and in water and compared to simulation results. The results are shown in Fig.12 where a sharp resonance is seen at 433.92MHz by the dip in the return loss plot which matches simulation. *The operational 10dB bandwidth of the UWA design is shown in Fig.13 which confirms a bandwidth of 40MHz, more than sufficient to accommodate typical wideband modulation standards such as WiFi.* Fig.14 shows the fabricated design next to a computer mouse as a size reference.

4.2 Bianisotropic Metasurface Design

In this section, we describe how METALINK improves the FoV of the water-air RF communication channel by designing a bianisotropic metasurface that goes beyond Snell's law. Moreover, due to its fully passive nature, METALINK does not require any power sources, facilitating effortless deployment and installation on fresh water bodies.

4.2.1 ***How to go beyond the forbidden region?*** Snell's law (Sec.3.1) can be expanded to what is known as the Generalized Snell's Law [111, 113]:

$$n_t sin(\theta_t) - n_i sin(\theta_i) = \frac{\lambda_o}{2\pi}\frac{d\Phi}{dz} \qquad (13)$$

where $\frac{d\Phi}{dz}$ is the phase gradient along the z axis using Fig.2. The linear phase gradient at the boundary between two mediums imparts a
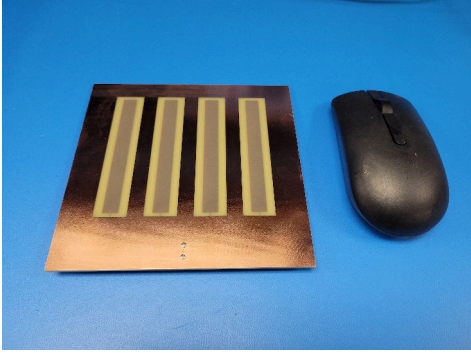
Figure 14: UHF Phased Array

shift in the transverse wave-number *i.e.,* $\beta_t = \beta_z + \frac{d\Phi}{dz}$ [19]. The transmitted wave-number, $\vec{\beta}_t$, which must satisfy $\sqrt{\beta_y^2 + \beta_z^2}$, now has an expanded range of possible solutions *i.e.,* $\{\beta_t(1 - \frac{d\Phi}{dz}), \beta_t(1 + \frac{d\Phi}{dz})\}$. This means that evanescent waves which were once bound in the forbidden region, can be converted into propagating ones. As shown in Fig.15, by generating phase gradients at the air and water boundary, the initial FoV depicted by the blue curve shifts, allowing incident angles of 10, 20 and 30° from water to refract to 0° in air. *To summarize, by combining multiple phase gradient metasurfaces, the FoV can be expanded, allowing signals to propagate across the air-water medium freely.*

*4.2.2 **Why do we need bianisotropy?*** Generating a phase gradient, $\frac{d\Phi}{dz}$, requires specially designed structures which can exhibit localized phase control of the incident EM waves. In addition to phase control, the metasurface must not induce reflections of its own at the boundary. To achieve this, we need to design a metasurface with correct input and output impedances in order to properly match the two mediums on either side [8, 105]. Previous designs [10, 60, 66, 73] were not able to simultaneously produce lossless, passive, and reflection-less transformations for different input and output impedances. To achieve all three requirements, bianisotropy is required [21] which gives meta-surface designs more degrees of freedom compared to non-bianisotropic designs.

*4.2.3 **How to calculate the required phases?*** To attain the required phase gradient while ensuring proper matching impedances for FoV expansion, we examine the required boundary conditions for the metasurface by applying Eq.(4) to determine the required impedances of the metasurface. The resultant phase gradient can be extracted from the calculated impedances as [21]:

$$Z = -j\{\frac{1}{2}Im\{\frac{E_{1,x} + E_{2,x}}{H_{2,y} - H_{1,y}}\} + K_{em}Im\{\frac{E_{2,x} - E_{1,x}}{H_{2,y} - H_{1,y}}\}\} \quad (14)$$

$$Y = -j\{\frac{1}{2}Im\{\frac{H_{1,y} + H_{2,y}}{E_{2,x} - E_{1,x}}\} - K_{em}Im\{\frac{H_{2,y} - H_{1,y}}{E_{2,x} - E_{1,x}}\}\} \quad (15)$$

$$K_{em} = \frac{1}{2}\frac{Re(E_{2,x}H_{1,y} - E_{1,x}H_{2,y})}{Re\{(E_{2,x} - E_{1,x})(H_{2,y} - H_{1,y})\}} \quad (16)$$

where H, Z, Y and K_{em} are the magnetic field (*i.e., E/η*), electrical impedance, magnetic admittance and the magneto-electric coupling coefficient, a requirement for bianisotropy. We refer interested readers to the detailed derivation to [7, 21, 68] for more information.

Using Eq.(14)-(16), we calculate the required phase distribution on the air/water boundary for incident signals in water arriving
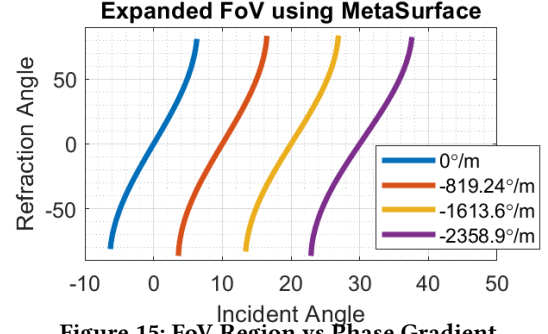

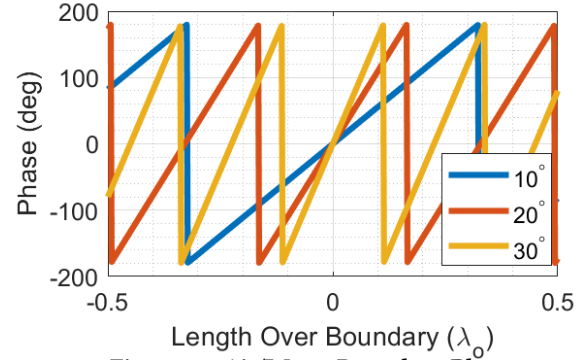**Figure 15: FoV Region vs Phase Gradient.**

Figure 16: Air/Water Boundary Phase.

at 10, 20 and 30° and refracting in air to 0°. As seen in Fig.16, the phase gradient requires metasurfaces of various sizes which can provide full 360° phase control over the air-water boundary. Furthermore, as the incident angle increases, the phase gradient requires smaller metasurfaces which can achieve the 360° phase response. For example, a metasurface measuring $2\times0.11\lambda_o \approx 153mm$ is required to achieve refraction in air from a 30° incident wave. The size requirement of the metasurface for air-water refraction poses a unique challenge.

*4.2.4 **How to design the meta-atom?*** The results discussed in the previous section assumes continuous phase gradients on the air/water boundary. For ease of metasurface design and fabrication, we discretize the boundary such that a sufficient number of "meta-atoms" can approximate the phase gradient. Each meta-atom will impart a desired phase shift at the location on the air/water boundary following Fig.16. While discretization is necessary, there are inherent limits. Too few meta-atoms can lead to high losses across the metasurface [25, 87]. Conversely, an excessive number of meta-atoms presents a design challenge, as it necessitates a reduction in the size of each meta-atom.

To achieve sufficiently small meta-atoms, we investigate two main types, single-layer designs and 3D-all-dielectric. Single-layer designs consist of specially configured metallic or dielectric patterns which can induce phase shifts to impinging EM waves[25, 107]. However, a major drawback is that they cannot readily exhibit the bianisotropic response due to the lack of multiple DoF. *At a minimum, three DoFs are required to achieve proper impedance matching and phase control* [14, 21]. More importantly, the required sizes are too large to satisfy the accuracy of the discretization at UHF frequencies [59, 66, 87]. 3D-all-dielectric materials can consist of
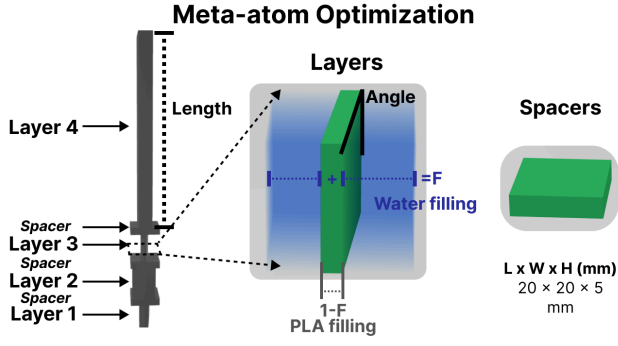
Figure 17: Meta-Atom Design Using 4 Layers.

multiple layers or arbitrary 3D structures. These designs can can provide many degrees of freedom [54] due to the ability to add more layers or increase the structure complexity. In addition, they can be easily fabricated using 3D-printing techniques[9, 14, 52, 79]. Taking inspiration from [19, 65, 70, 79, 108], we design a new meta-atom which can achieve ultra-small scale dimensions by leveraging the large refractive index of water.

The METALINK meta-atom consists of PLA rectangles surrounded by water as shown in the figure of Fig.17. PLA is a cheap, easy to prototype material that is stable in water environments for long durations [83]. By adjusting the filling factor between PLA and water, an effective permittivity $\epsilon_{x,y}$ for the x/y-polarized EM wave can be modeled as:

$$\epsilon_x = f\epsilon_{water} + (1-f)\epsilon_{air}, \epsilon_y = \left(\frac{f}{\epsilon_{water}} + \frac{(1-f)}{\epsilon_{air}}\right)^{-1} \quad (17)$$

where f is the filling factor. This approximation is valid for subwavelength designs (*i.e.,* size≪λ_o)[79]. The variable permittivity can be used to adjust the impedance of the meta-atom on either side. These rectangles form the building block of the METALINK metasurface. Multiple layers of PLA structures can be combined to achieve a desired EM response by carefully selecting the meta-atom geometries of each layer.

Since the permittivity of each layer can be calculated using a closed form expression (Eq.(17)), wave-matrices (WMs) can be used to calculate the response of the entire multi-layer structure [20, 78, 79, 107, 110]. The WM for a multi-layer structure is found as follows [79]:

$$M_t = \prod_{i=1}^{N}(I \otimes R(\sin\theta_i))M_i^{ansio}(I \otimes R(\sin\theta_i))^T M_i^{iso} \quad (18)$$

where I, $\otimes$, R, θ, M_i^{ansio}, and M_i^{iso} are the 2×2 identity matrix, Kronecker product, rotation matrix, rotation angle, WM for the anisotropic layer, and the WM of the isotropic layer (*i.e.,* spacer). The WMs for the anisotropic and spacer layers are calculated using [78]:

$$M_{ansio} = M_{inter}^1 M_{delay} M_{inter}^2 \quad (19)$$

$$M_{delay} = \sum_{x,y}\begin{bmatrix} e^{j\beta_0 d\sqrt{\epsilon_{x,y}}} & 0 \\ 0 & e^{-j\beta_0 d\sqrt{\epsilon_{x,y}}} \end{bmatrix} \otimes \begin{bmatrix} 1_x/0_y & 0 \\ 0 & 0_x/1_y \end{bmatrix}$$

$$M_{inter} = \sum_{x,y}\frac{1}{T_{x,y}}\begin{bmatrix} 1 & R_{x,y} \\ R_{x,y} & 1 \end{bmatrix} \otimes \begin{bmatrix} 1_x/0_y & 0 \\ 0 & 0_x/1_y \end{bmatrix}$$

where M_{inter}, M_{delay}, d, $T_{x/y}$, and $R_{x/y}$ are the interface WM on either side, phase delay through the layer, thickness of the layer,
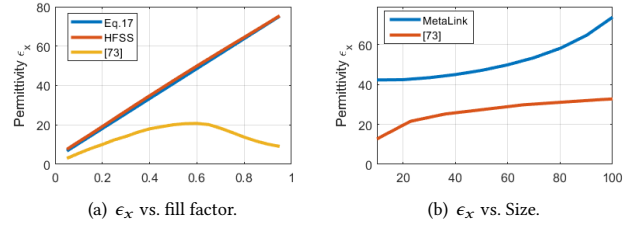

Figure 18: Permittivity Comparison

and the Fresnel coefficients. The equations in Eq.(19) are derived by applying the Fresnel coefficients to each medium boundary and by applying Maxwell's continuity equations to each medium, allowing for matrix multiplication of the fields from one medium to the next [91].

To demonstrate the permittivity control of the METALINK meta-atom, we simulate the S parameters of a single layer using HFSS and calculate the permittivity using [6]. The meta-atom x/y = 20mm with d = 30mm. We also compare our design to [79] to demonstrate the novel ultra-small scale performance of METALINK. In Fig.18(a), the METALINK meta-atom matches the closed-form expression in Eq.(17) whereas the design in [79] fails to meet the expected permittivity values. We further compare the two designs by sweeping the size of the meta-atoms with $f = 0.5$, and $d = 30$mm. In Fig.18(b), we see that our design approaches the expected permittivity as the meta-atom size decreases whereas the design in [79] does not achieve the permittivity, even for sizes beyond 100mm. *Therefore, the approach in [79] cannot be used at ultra-sub-wavelength scales whereas METALINK can since it can be approximated by the closed form expression [93, 101, 110].* Furthermore, as the height of the meta-atom is varied with fixed f and d, the permittivity should maintain the same value. However, in Fig.19(a), we see that the [79] design is not stable.

4.2.5 ***Optimizing the metasurface structure*** Determining the desired response given many variables requires the use of a numerical optimizer unless closed form expressions can be derived [13, 91]. Given that at least 3 DoFs are required, METALINK must use at least 3 layers. In addition, for each layer we must define the thickness, rotation, and filling factor in order to achieve a desired response. For METALINK we adopt a four layer structure with three spacers as shown in the left figure of Fig.17. Each spacer has a fixed geometry, whereas the four anisotropic layers are optimized for thickness, rotation and filling factor. To maintain a fixed height of 20cm for all meta-atoms, we set the height of the last layer as $20cm - 3d_{spacer} - \sum(d_{1,2,3})$.

The optimization function calculates the cost of a design and iterates until the cost function is minimized given some criteria.
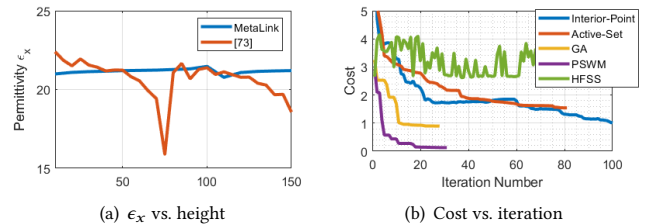

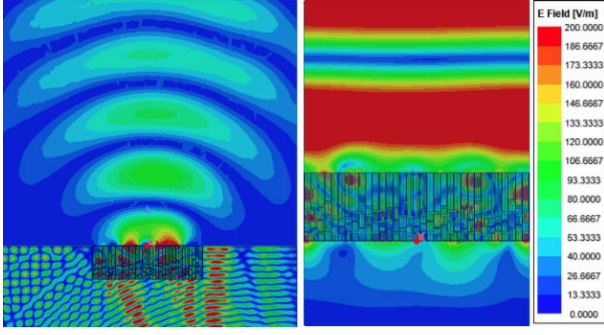**Figure 19: Permittivity and Optimizer comparison**

Figure 20: Metasurface Simulation in HFSS

The cost function used is as follows:

$$cost = \sum_{1,2} |S_{xx}| + |S_{21} - S_{21d}| + 15 \frac{|ang(S_{21}) - \phi_d|}{\pi} \qquad (20)$$

where S_{xy}, S_{xyd}, ϕ_d are the scattering parameters (S-parameters), the desired S-parameters, and the desired phase shift. They can be calculated from the WM in Eq.(18) by following the method described in [79]. The meta-surface is designed to satisfy 20MHz of bandwidth using Eq.20.

Using the cost function in Eq.(20), we compare non-linear optimizers such as gradient-descent and genetic algorithms such as differential-evolution and particle-swarm (PSWM) optimization. For each optimizer we set the desired phase to 0. The cost function forces the solver to minimize the return loss and maximize the transmission coefficient. The cost vs. iteration is shown in Fig.19(b). The PSWM reached a minimum in fewer iterations compared to the others such as HFSS which could not converge. Interior-point took more iterations than the rest however, it was the fastest in terms of clock time. The resulting CPU times for all five options were 419, 251, 1518, 740, and 7200s. Due to the speed, we opt for interior-point optimization to find the optimal geometries for all meta-atom designs. Interior-point optimization is used to find optimal geometries for impedance matching and phases ranging from $180°$ to $-165°$ in steps of $15°$ which is sufficient to ensure sufficient sampling of the boundary conditions. Using the optimal METALINK meta-atoms, we simulate a design which refracts an incident $-20°$ wave in water to $0°$ in air using HFSS. The plane-wave propagating into the air is seen in the left figure of Fig.20 while the fields below the metasurface are undisturbed, implying minimal reflections. In addition, we simulate the metasurface design using periodic boundary conditions and remove the water environment below the metasurface. As shown in the right figure of Fig.20, an evanescent wave is produced below the metasurface when the water medium is absent. This confirms that the metasurface is imparting a shift to the transverse wave-number, allowing evanescent waves to become propagating ones by generating one of its own.

5 Implementation and Evaluation

5.1 Implementation

The METALINK deployment primarily includes a custom UWA, a 3D printed bianisotropic all-dielectric metasurface, an air antenna [5], a USRP B210 [80], and a KeySight Spectrum analyzer [56]. We acquired an experimental license from the FCC to conduct experiments within the 418.92 MHz to 448.92 MHz band. **Transmit-**
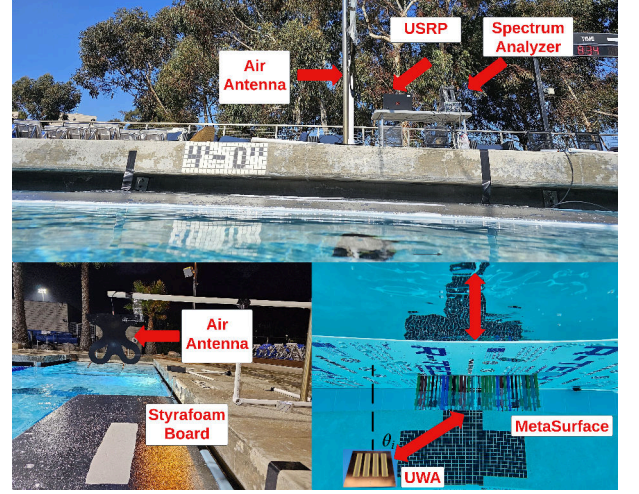

Figure 21: Experimental Setup

ter and Receiver. The USRP B210 is used as a transmitter. Using GNURadio [37], we send 20MHz OFDM WiFi packets centered at 433.92MHz through the air or through water by connecting the B210 to the corresponding antenna. The OFDM symbol consists of 64 subcarriers which covers the entire 20MHz frequency span. Throughout all measurements, the B210 is continuously transmitting packets and captured using a Keysight spectrum analyzer for analysis. Using the B210 as an air transmitter, the effective isotropic radiated power (EIRP) of the setup is $EIRP = 16dBm + 3dB = 19dBm$, where 16dBm is the output power of the B210 and 3dB is the gain of the COTS UHF antenna, well below the FCC limit [35]. Using the spectrum analyzer, the effective noise floor is $NoiseFloor = -174dBm/Hz + 10log10(20MHz) + NF_c = -97dBm$. NF_c is the cascaded noise figure of the analyzer which is $NF = 3.95dB$ [55].

METALINK Metasurface. After fabrication of each METALINK meta-atom, we organize them following the phase requirements of Sec.4. To prevent misalignment between meta-atoms, we place 1.6mm thin balsa wood sheets between adjacent meta-atoms in the linear array. As shown in Fig.21, the METALINK metasurface is completely submerged under the air/water boundary. To enforce metasurface's vertical flotation position on the waterline, we tape the top of the metasurface array to the bottom of a Styrofoam board. As a result, the metasurface flotation is exactly perpendicular to the water surface. To reduce diffraction effects, the board is covered with a thin metallic film, and a rectangular opening the size of the array is cut out [107]. The cost of each meta-atom is approximately $0.8 dollars.

Antennas. Thanks to water's high dielectric constant, UW antennas can be designed much smaller, enabling phased array configurations. In contrast, UHF antennas in air are significantly larger, which limits their achievable gain. Consequently, the antenna gains for air and UWA at 433.92 MHz are 3 dB and 13 dB, respectively [5]. Each antenna is matched to 50 Ohms which allows for either TX or RX operation. The air antenna (Fig.21) is fixed on a PVC pole 1 meter above the water surface for all measurements. The UWA (Sec.4) faces the METALINK metasurface from underneath to send or receive WiFi packets. The fabrication cost of the UWA is $200 dollars.
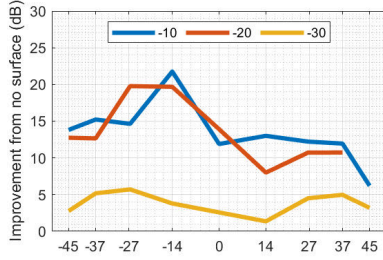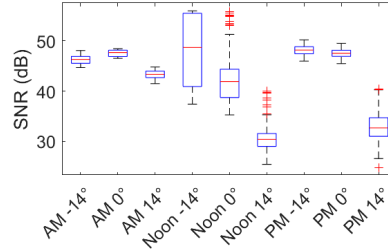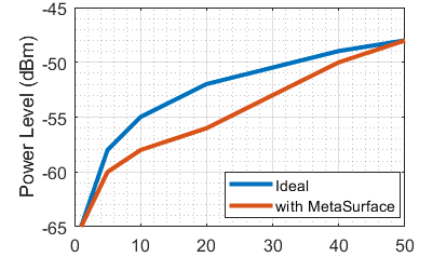
Figure 22: Antenna Patterns (deg)

Figure 23: Time of Day

Figure 24: Bandwidth (MHz)

5.2 Evaluation

Measurements were conducted in a public swimming pool during normal hours where swimmers were allowed to exercise around the experimental setup. The public pool provides two areas for evaluating METALINK, a shallow end with a depth of 1.2m and a deep end with a depth of 4.3m. All measurements were conducted in the shallow end except for the peak range measurement which was conducted in the deep end. In addition, we focus on the channel between TX signals in water to an air RX due to the severe restraints discussed in Sec.3. Evaluation metrics such as received signal strength (RSS) and signal-to-noise ratio (SNR) were captured using the receiver. The SNR values contain real-world hardware impairments due to the receiver and transmitter. Data-rates are then provided using the MCS lookup table [104] for single spatial stream 20MHz WiFi. Measurements that contain box plot information were conducted using 1001 points measured over a 10s period.

*5.2.1 **Metasurface Refraction Patterns*** Three meta-surfaces were constructed to refract signals from -10,-20,-30° in water to 0° in air which allows for aerial communications as nodes fly over the metasurface. Each surface consisted of 22, 11, and 8 meta-atoms respectively, following Sec.4.2 for the required phase discretization. The air antenna was used as a transmitter while the UWA was positioned underneath the metasurface at a depth of 1.5m acting as a UW sensor node. The UWA was then placed at various angles to measure the refraction pattern. The results of the antenna patterns are plotted in Fig.22.

When a metasurface is positioned at the boundary between air and water, notable peaks emerge at approximately 14° and 20°. These peaks exhibit a strength that is 20dB higher compared to scenarios where no metasurface is employed. This enhancement is observed when using metasurfaces originally designed for refraction angles of -10° and -20° respectively. These strong peaks indicate that the metasurface is concentrating power at those directions. For the design intended to refract the WiFi signal towards -30°, we see a small improvement over the no-surface case. We believe that the reduction in performance can be attributed to the limited scan-angle stability of the meta-atom design. Improvements in height reduction can mitigate these issues and further improve the FoV. Overall, measured FoV is improved by 5× due to the ability to communicate at angles beyond Snells Law.

*5.2.2 **Time of Day.*** To verify the stability of the METALINK metasurface and UWA versus temperature fluctuations, we conduct experiments at three different times of the day *i.e.,*, morning, afternoon and night. Due to the temperature variations (*i.e.,* 15.5-26.6°C)

throughout the day, the water temperature will change, impacting the EM properties of water and thus, the performance of the metasurface and UWA. Conductivity however, does not change the frequency response of the UWA and metasurface, but changes the amplitude response of the wireless channel. Using the surface designed for -10° refraction, we measure the RSS at three points near the desired direction, -14°, 0°, and 14°, as shown in Fig.23. The average values seen across all times of the day are stable, indicating our UWA and surface design were not impacted by the temperature swing. The large variance that is seen during the "Noon" measurements is due to radio interference caused by HAM operators which use the 433.92MHz band [35].

*5.2.3 **Bandwidth*** To evaluate the bandwidth (BW) performance of the METALINK metasurface, we capture the WiFi spectrum using a METALINK surface design that refracts to -20°. The UWA is used as the transmitter, placed at -20° underwater, while the receiver captures the WiFi signal in the air at 0°. At a BW of 50MHz we integrate the power within the channel as shown in Fig.24, which is $\approx -48 dBm$. The extended BW includes noise and interference sources. As the integration BW is reduced, the resulting total channel power is plotted and compared to an ideal flat-top WiFi spectrum. The difference between the ideal integrated power and the calculated one determines the bandwidth symmetry of the METALINK metasurface. For bandwidths near 20MHz, power is reduced by 4dB, implying spectrum roll off.

As the BW is reduced to 1MHz, the ideal and calculated increasingly match. To improve the BW performance of METALINK, more layers could be added to provide more DoFs which could allow for optimization to be performed over a wide bandwidth (*i.e.,* 40, or 80MHz).

*5.2.4 **Surface Wave Interference*** To validate the practicality of METALINK in underwater environments, we conduct experiments to test the link robustness in the presence of surface waves. The same -20° metasurface design is used where the UWA acts as a transmitter. The UWA was placed at the bottom of the pool floor approximately 2m below the air antenna. A swimmer is then asked to create surface waves by oscillating in an up and down motion near the surface. We tested the link with small surface waves, enough to cause a rocking motion in the Styrofoam structure. Second, we ask the swimmer to generate large waves, enough to cause water to overtake the foam board. The results are shown in Fig.25. The SNR maintains an average value of 39dB in all three scenarios due to the stability of the structure, but also due to the fairly large beamwidth that is generated in the underwater environment. For much larger metasurfaces, which create narrower beamwidths, surface waves
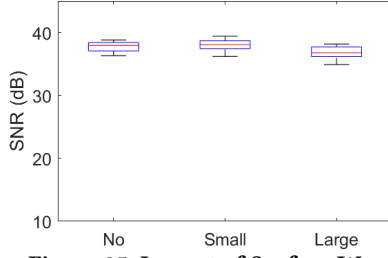
Figure 25: Impact of Surface Waves

Figure 26: SNR vs. Distance (m)

Figure 27: Curve Fitted Distance

could impact the stability of the antenna pointing. To mitigate this issue, fan beam designs could be leveraged to increase antenna pointing stability [69]. Lastly, with the underwater, phased array antenna pointing did not impact the SNR due to surface waves because of the sufficiently large beamwidth. Strict alignment between underwater nodes and the metasurface is unnecessary since the antenna has a 25° beamwidth, providing 12.5m of horizontal coverage at 29m of depth.

5.2.5 **Distance** To validate METALINK's maximum range, experiments are conducted up to 4.3m (limited by pool dimensions) using a 22 meta-atom design that refracts signals to -20° by combining two 11 meta-atom designs. RSS is measured at 0.75m intervals along the -20° trajectory from the water line, with the air antenna positioned 1m above the water and 0° above the metasurface. RSS is collected using both air and UW antennas as transmitters to confirm bi-directional performance, with results plotted in Fig.26. The gradual drop in SNR suggests minimal water loss, with signal attenuation similar to that of Fig.6 which used a $\tan(\delta) = 0.01$, indicating a chlorinated pool with minimal conductivity [36] and a loss tangent less than $\tan(\delta) = 0.01$. In terms of frequency selectivity, the water environment experiences significant multi-path reflections due to pool walls, large air/water boundaries, and surrounding structures, resulting in large amplitude variations vs distance which is also seen in Fig.5.

Due to pool size constraints, we determine maximum range by fitting our measurement setup parameters into the channel model from Section 3. Using data collected with the air TX antenna, we curve fit the data with $\tan \delta = 0.003$ or an attenuation coefficient of ~1dB/m. Figure 27 shows simulated RSS versus distance for our fitted data at 433.92MHz and 2.4GHz. The simulation predicts a range of 29 meters, which is 7.9× larger than what a 2.4 GHz WiFi device could achieve without a metasurface. Without a metasurface, SNR loss of 20dB (Figure 22) would reduce the range to 11m at 433.92MHz, limiting the FoV to 13°. The 2.4GHz link would drop to ~cms of range as confirmed in [107]. Increasing the EIRP of the METALINK transmitter to the FCC limit of 36 dBm would enable larger transmission distances. Furthermore, considering water's high attenuation, health concerns related to specific absorption rate [34] are minimized, allowing for potential future increases to FCC EIRP limits.

6 Discussion and Future Work

Water EM parameters: METALINK works best in fresh water systems with low conductivity. In marine environments, which are
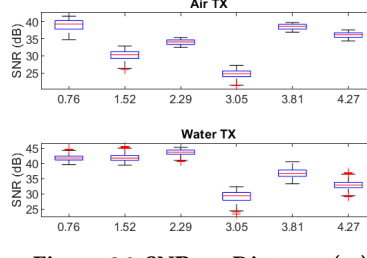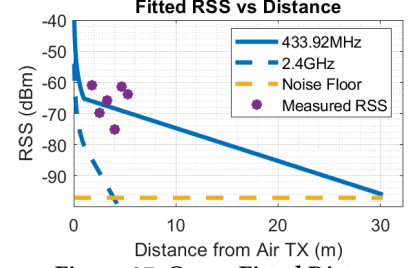
more conductive, using lower frequencies and commercially available RF PAs is warranted. In these waters, there's a trade-off between data rate and distance: higher data rates need wider bandwidth, which requires higher frequencies, but leads to more attenuation over long distances. New meta-materials designed to work at ultra-low frequencies while staying compact can significantly enhance underwater communication with air nodes.

Sensor Integration: With an additional depth sensor, the modulation scheme can adapt to the frequency selectivity through the water medium. Previous models [72, 75, 81, 103, 116] have shown that the water properties at multiple depths can be estimated by sensing the water properties at a single depth. Using these models, proper modulation order can be selected to optimize the water channel link. Similarly, data collected in air of the water boundary, can be used to predict the water properties at great depths below the water surface.

TX/RX node mobility: Given METALINK's ability to model arbitrary bi-directional refraction, 2D arrays can be formed by combining the designs in Fig. 22, giving mobile nodes, in both water and air, the freedom to move around without refraction or pointing errors. For versatile deployment, multiple metasurfaces can form a joint metasurface, improving connectivity from multiple angles up to an FoV of 2×70 [105]. Full 3D mobility could open the door for various applications such as localization, remote sensing, and diver communications to airborne nodes.

7 Conclusion

This paper presents METALINK, an end-to-end RF cross-medium platform that enables underwater systems to directly communicate with airborne systems using existing RF technologies. By adding a naturally floating ultra-small form factor metasurface to the water-air boundary, reflection and refraction that previously hinders RF communication/sensing application is now removed. METALINK's novel UWA design further expands underwater communication distance up to 29 meters. METALINK technology can take common wireless communications such as WiFi, to other domains using cross-medium interfaces.

Acknowledgments

References

[1] A A Abdou, A Shaw, A Mason, A Al-Shamma'a, J Cullen, S Wylie, and M Diallo. A matched bow-tie antenna at 433mhz for use in underwater wireless sensor networks. *Journal of Physics: Conference Series*, 450:012048, 2013.

[2] Fernando López Aguilar, Gorka Rubio Cidre, José Manuel López López, and Javier Regidor Paris. Mutual information effective snr mapping algorithm for fast link adaptation model in 802.16e. In Periklis Chatzimisios, Christos Verikoukis, Ignacio Santamaría, Massimiliano Laddomada, and Oliver Hoffmann, editors, *Mobile Lightweight Wireless Systems*, pages 356–367, Berlin, Heidelberg, 2010. Springer Berlin Heidelberg.

[3] Adam R. H. Alhawari, Sama F. Majeed, Tale Saeidi, Sajid Mumtaz, Hisham Alghamdi, Ayman Taher Hindi, Abdulkarem H. M. Almawgani, Muhammad Ali Imran, and Qammer H. Abbasi. Compact elliptical uwb antenna for underwater wireless communications. *Micromachines*, 12(4), 2021.

[4] Ansys. Ansys hfss best-in-class 3d high frequency structure simulation software.

[5] AppliedEMInnovations. Broadband vivaldi antenna 400 mhz to 8 ghz.

[6] S. Arslanagić, T. V. Hansen, N. A. Mortensen, A. H. Gregersen, O. Sigmund, R. W. Ziolkowski, and O. Breinbjerg. A review of the scattering-parameter extraction method with clarification of ambiguity issues in relation to metamaterial homogenization. *IEEE Antennas and Propagation Magazine*, 55(2):91–106, 2013.

[7] V. S. Asadchy, M. Albooyeh, S. N. Tcvetkova, A. Díaz-Rubio, Y. Ra'di, and S. A. Tretyakov. Perfect control of reflection and refraction using spatially dispersive metasurfaces. *Phys. Rev. B*, 94:075142, Aug 2016.

[8] Viktar S. Asadchy, Ana Díaz-Rubio, and Sergei A. Tretyakov. Bianisotropic metasurfaces: physics and applications. *Nanophotonics*, 7(6):1069–1094, 2018.

[9] Technology Assessment and Transfer. Additive manufacturing / 3d printing.

[10] Vasileios G. Ataloglou, Michael Chen, Minseok Kim, and George V. Eleftheriades. Microwave huygens' metasurfaces: Fundamentals and applications. *IEEE Journal of Microwaves*, 1(1):374–388, 2021.

[11] AusCTW. High-speed underwater acoustic communications – challenges and solutions.

[12] Mary Bellis. The history of sonar.

[13] Annemarie Berkhout and A. Femius Koenderink. A simple transfer-matrix model for metasurface multilayer systems. *Nanophotonics*, 9(12):3985–4007, 2020.

[14] Ke Bi, Qingmin Wang, Jianchun Xu, Lihao Chen, Chuwen Lan, and Ming Lei. All-dielectric metamaterial fabrication techniques. *Advanced Optical Materials*, 9(1), 2020.

[15] Eun Bok, Jong Jin Park, Haejin Choi, Chung Kyu Han, Oliver B. Wright, and Sam H. Lee. Metasurface for water-to-air sound transmission. *Phys. Rev. Lett.*, 120:044302, Jan 2018.

[16] Newbold J.D. Bott T.L. A multi-year analysis of factors affecting ecosystem metabolism in forested and meadow reaches of a piedmont stream. *Hydrobiologia*, 850:4243–4269.

[17] Lloyd Butler. Underwater radio communication.

[18] Charles J. Carver, Zhao Tian, Hongyong Zhang, Kofi M. Odame, Alberto Quattrini Li, and Xia Zhou. AmphiLight: Direct Air-Water communication with laser light. In *17th USENIX Symposium on Networked Systems Design and Implementation (NSDI 20)*, pages 373–388, Santa Clara, CA, February 2020. USENIX Association.

[19] Hamid Akbari Chelaresi, Pooria Salami, and Leila Yousefi. Evanescent-to-propagating wave conversion using continuous high-order dielectric metasurfaces. In *2021 29th Iranian Conference on Electrical Engineering (ICEE)*, pages 831–835, 2021.

[20] Hou-Tong Chen, Jiangfeng Zhou, John F. O'Hara, Frank Chen, Abul K. Azad, and Antoinette J. Taylor. Antireflection coating using metamaterials and identification of its mechanism. *Phys. Rev. Lett.*, 105:073901, Aug 2010.

[21] Michael Chen, Elena Abdo-Sánchez, Ariel Epstein, and George V. Eleftheriades. Theory, design, and experimental verification of a reflectionless bianisotropic huygens' metasurface for wide-angle refraction. *Phys. Rev. B*, 97:125433, Mar 2018.

[22] Peng Chen, Yue Rong, Sven Nordholm, Zhiqiang He, and Alexander J. Duncan. Joint channel estimation and impulsive noise mitigation in underwater acoustic ofdm communication systems. *IEEE Transactions on Wireless Communications*, 16(9):6165–6178, 2017.

[23] Tuochao Chen, Justin Chan, and Shyamnath Gollakota. Underwater messaging using mobile devices. In *Proceedings of the ACM SIGCOMM 2022 Conference*, SIGCOMM '22, page 545–559, New York, NY, USA, 2022. Association for Computing Machinery.

[24] Zhipeng Chen, Zhiqiang He, Kai Niu, and Yue Rong. Neural network-based symbol detection in high-speed ofdm underwater acoustic communication. In *2018 10th International Conference on Wireless Communications and Signal Processing (WCSP)*, pages 1–5, 2018.

[25] Hongchen Chu, Haoyang Zhang, Yang Zhang, Ruwen Peng, Mu Wang, Yang Hao, and Yun Lai. Invisible surfaces enabled by the coalescence of anti-reflection and wavefront controllability in ultrathin metasurfaces. *Nature Communications*, 12(1), 2021.

[26] Devin Coldewey. Finally, an underwater messaging app.

[27] Balanis A. Constantine. *Antenna theory: Analysis and Design.* Wiley, 2016.

[28] John Coonrod. A practical guide to the design of microstrip antenna arrays.

[29] Thierry Deschamps de Paillette, Alain Gaugue, Emmanuel Parlier, and Sylvain Dardenne. Antenna design for underwater wireless telemetry systems. In *2017 11th European Conference on Antennas and Propagation (EUCAP)*, pages 2251–2255, 2017.

[30] Ayman H. Dorrah, Michael Chen, and George V. Eleftheriades. Bianisotropic huygens' metasurface for wideband impedance matching between two dielectric media. *IEEE Transactions on Antennas and Propagation*, 66(9):4729–4742, 2018.

[31] Minimize Microstrip Radiation Effects. The radiation of electromagnetic power by microstrip configurations. *IEEE Transactions on Microwave Theory and Techniques*, 25(9):719–725, 1977.

[32] Electro-Voice. Uw30.

[33] electronicsnotes. Wi-fi channels, frequencies, bands and bandwidths.

[34] fcc. Cell Phones and Specific Absorption Rate.

[35] FCC. Fcc online table of frequency allocations.

[36] Yonas A. Gezahegn, Juming Tang, Shyam S. Sablani, Patrick D. Pedrow, Yoon-Ki Hong, Huimin Lin, and Zhongwei Tang. Dielectric properties of water relevant to microwave assisted thermal pasteurization and sterilization of packaged foods. *Innovative Food Science and Emerging Technologies*, 74:102837, 2021.

[37] GNU Radio Website, accessed February 2012.

[38] Andrei Grebennikov. Power combiners, impedance transformers and directional couplers: Part ii.

[39] Hongzhi Guo, Zhi Sun, and Pu Wang. On reliability of underwater magnetic induction communications with tri-axis coils. In *ICC 2019-2019 IEEE International Conference on Communications (ICC)*, pages 1–6. IEEE, 2019.

[40] WS Hampshire. What is fr4 material?

[41] Tong Hao, Wuan Zheng, Wenchao He, and Kaiqiang Lin. Air-ground impedance matching by depositing metasurfaces for enhanced gpr detection. *IEEE Transactions on Geoscience and Remote Sensing*, 58(6):4061–4075, 2020.

[42] D.A. Hill, D.G. Camell, K.H. Cavcey, and G.H. Koepke. Radiated emissions and immunity of microstrip transmission lines: theory and reverberation chamber measurements. *IEEE Transactions on Electromagnetic Compatibility*, 38(2):165–172, 1996.

[43] Roger Hill. A practical guide to the design of microstrip antenna arrays.

[44] John S. Ho, Brynan Qiu, Yuji Tanabe, Alexander J. Yeh, Shanhui Fan, and Ada S. Y. Poon. Planar immersion lens with metasurfaces. *Phys. Rev. B*, 91:125145, Mar 2015.

[45] Mark Hoferitza. Using rf technology to form a wireless network under water.

[46] Michael Horodynski, Matthias Kühmayer, Clément Ferise, Stefan Rotter, and Matthieu Davy. Anti-reflection structure for perfect transmission through complex media. *Nature*, 607(7918):281–286, 2022.

[47] Yueqiang Hu, Xudong Wang, Xuhao Luo, Xiangnian Ou, Ling Li, Yiqin Chen, Ping Yang, Shuai Wang, and Huigao Duan. All-dielectric metasurfaces for polarization manipulation: Principles and emerging applications. *Nanophotonics*, 9(12):3755–3780, 2020.

[48] Zhandong Huang, Shengdong Zhao, Yiyuan Zhang, Zheren Cai, Zheng Li, Junfeng Xiao, Meng Su, Qiuquan Guo, Chuanzeng Zhang, Yaozong Pan, Xiaobing Cai, Yanlin Song, and Jun Yang. Tunable fluid-type metasurface for wide-angle and multifrequency water-air acoustic transmission. *Research*, 2021.

[49] hydrointernational. Technology in focus: Underwater electromagnetic propagation.

[50] S. I. Inácio, M. R. Pereira, H. M. Santos, L. M. Pessoa, F. B. Teixeira, M. J. Lopes, O. Aboderin, and H. M. Salgado. Antenna design for underwater radio communications. In *OCEANS 2016 - Shanghai*, pages 1–6, 2016.

[51] Maen Ishtaiwi, Muna Hajjyahya, and Shahd Habbash. Electrical properties of dead sea water. *Journal of Applied Mathematics and Physics*, 09(12):3094–3101, 2021.

[52] Saman Jahani and Zubin Jacob. All-dielectric metamaterials. *Nature Nanotechnology*, 11(1):23–36, 2016.

[53] Jonathan H Jiang and Dong L Wu. Ice and water permittivities for millimeter and sub-millimeter remote sensing applications. *Atmospheric Science Letters*, 5(7):146–151, 2004.

[54] Muamer Kadic, Graeme W. Milton, Martin van Hecke, and Martin Wegener. 3d metamaterials. *Nature Reviews Physics*, 1(3):198–210, 2019.

[55] keysight. Keysight n9933b.

[56] keysight. Pna-l network analyzers.

[57] Gyoungdeuk Kim and Sangkil Kim. Design and analysis of dual polarized broadband microstrip patch antenna for 5g mmwave antenna module on fr4 substrate. *IEEE Access*, 9:64306–64316, 2021.

[58] Minseok Kim and George V. Eleftheriades. Design and experimental demonstration of impedance-matched circular-polarization-selective surfaces with spin-selective phase modulations. *Phys. Rev. Appl.*, 13:014009, Jan 2020.

[59] Ali Lalbakhsh, Muhammad U. Afzal, Touseef Hayat, Karu P. Esselle, and Kaushik Mandal. All-metal wideband metasurface for near-field transformation of medium-to-high gain electromagnetic sources. *Scientific Reports*, 11(1), 2021.

[60] Guillaume Lavigne and Christophe Caloz. Generalized brewster effect using

bianisotropic metasurfaces. *Opt. Express*, 29(7):11361–11370, Mar 2021.

[61] Yoonill Lee. Analysis of data rate vs. snr in mimo wireless communication systems. In *2018 IEEE International Conference on Electro/Information Technology (EIT)*, pages 0262–0266, 2018.

[62] Lin Li, Kan Yao, Zuojia Wang, and Yongmin Liu. Harnessing evanescent waves by bianisotropic metasurfaces. *Laser Photonics Reviews*, 14(12), 2020.

[63] Yuzhou Li, Shengnan Wang, Cheng Jin, Yu Zhang, and Tao Jiang. A survey of underwater magnetic induction communications: Fundamental issues, recent advances, and challenges. *IEEE Communications Surveys & Tutorials*, 21(3):2466–2487, 2019.

[64] Hanjiang Luo, Jinglong Wang, Fanfeng Bu, Rukhsana Ruby, Kaishun Wu, and Zhongwen Guo. Recent progress of air/water cross-boundary communications for underwater sensor networks: A review. *IEEE Sensors Journal*, 22(9):8360–8382, 2022.

[65] Andrea Massaccesi, Paola Pirinoli, Valentina Bertana, Giorgio Scordo, Simone Luigi Marasso, Matteo Cocuzza, and Gianluca Dassano. 3d-printable dielectric transmitarray with enhanced bandwidth at millimeter-waves. *IEEE Access*, 6:46407–46418, 2018.

[66] Mohammad Memarian and George V. Eleftheriades. Evanescent-to-propagating wave conversion in sub-wavelength metal-strip gratings. *IEEE Transactions on Microwave Theory and Techniques*, 60(12):3893–3907, 2012.

[67] Xiangdong Meng, Ruixuan Liu, Hongchen Chu, Ruwen Peng, Mu Wang, Yang Hao, and Yun Lai. Through-wall wireless communication enabled by a metalens. *Phys. Rev. Appl.*, 17:064027, Jun 2022.

[68] Nasim Mohammadi Estakhri and Andrea Alù. Wave-front transformation with gradient metasurfaces. *Phys. Rev. X*, 6:041008, Oct 2016.

[69] John Nolan, Kun Qian, and Xinyu Zhang. Ros: Passive smart surface for roadside-to-vehicle communication. In *Proceedings of the 2021 ACM SIGCOMM 2021 Conference*, SIGCOMM '21, page 165–178, New York, NY, USA, 2021. Association for Computing Machinery.

[70] Jun Rong Ong, Hong Son Chu, Valerian Hongjie Chen, Alexander Yutong Zhu, and Patrice Genevet. Freestanding dielectric nanohole array metasurface for mid-infrared wavelength applications. *Opt. Lett.*, 42(13):2639–2642, Jul 2017.

[71] Diana Oviedo-Vargas, Marc Peipoch, Scott H Ensign, David Bressler, David B Arscott, and John K Jackson. Advancing freshwater science with sensor data collected by community scientists. *Frontiers in Ecology and the Environment*, n/a(n/a):e2748.

[72] R. Pawlowicz. Key physical variables in the ocean: Temperature, salinity, and density.

[73] Carl Pfeiffer and Anthony Grbic. Metamaterial huygens' surfaces: Tailoring wave fronts with reflectionless sheets. *Phys. Rev. Lett.*, 110:197401, May 2013.

[74] Carl Pfeiffer and Anthony Grbic. Bianisotropic metasurfaces for optimal polarization control: Analysis and synthesis. *Phys. Rev. Appl.*, 2:044011, Oct 2014.

[75] S. Piccolroaz, S. Zhu, R. Ladwig, L. Carrea, S. Oliver, A. P. Piotrowski, M. Ptak, R. Shinohara, M. Sojka, R. I. Woolway, and D. Z. Zhu. Lake water temperature modeling in an era of climate change: Data sources, models, and future prospects. *Reviews of Geophysics*, 2024.

[76] DAVID M. POZAR. *Microwave engineering*. JOHN WILEY SONS, 2021.

[77] Anderson R. Ramos, Bruno C. Silva, Marisa S. Lourenço, Emanuel B. Teixeira, and Fernando J. Velez. Mapping between average sinr and supported throughput in 5g new radio small cell networks. In *2019 22nd International Symposium on Wireless Personal Multimedia Communications (WPMC)*, pages 1–6, 2019.

[78] Amin Ranjbar and Anthony Grbic. Analysis and synthesis of cascaded metasurfaces using wave matrices. *Phys. Rev. B*, 95:205114, May 2017.

[79] Amin Ranjbar and Anthony Grbic. Broadband, multiband, and multifunctional all-dielectric metasurfaces. *Phys. Rev. Appl.*, 11:054066, May 2019.

[80] Ettus Research. Ub210 kit.

[81] Kit Rutherford and Ian Jowett. Procedure for calculating water temperature.

[82] Pooria Salami and Leila Yousefi. Far-field subwavelength imaging using phase gradient metasurfaces. *Journal of Lightwave Technology*, 37(10):2317–2323, 2019.

[83] Ivana Salopek Čubrić, Goran Čubrić, and Vesna Marija Potočić Matković. Behavior of polymer materials exposed to aging in the swimming pool: Focus on properties that assure comfort and durability. *Polymers*, 13(15), 2021.

[84] Atlas Scientific. What is the typical water conductivity range?

[85] Stavros Georgakopoulos Shan Jiang. Electromagnetic wave propagation into fresh water. *Journal of Electromagnetic Analysis and Applications*, 03(7), 2011.

[86] C. E. Shannon and W. Weaver. The mathematical theory of communication.

[87] Abhishek Sharma and Alex M Wong. Bipartite dielectric huygens' metasurface for anomalous refraction. *Physica Scripta*, 98(11):115539, 2023.

[88] Tao Shu, Yang Zou, Qirun Fan, Tianjin Mei, Xiaoxiao Dai, Chen Liu, Mengfan Cheng, Lei Deng, Qi Yang, and Deming Liu. Seamless rate adaptation for wide snr range in fso systems based on rate compatible modulation. *Opt. Lett.*, 49(16):4658–4661, Aug 2024.

[89] J.P. Simpson, R.R. Goulette, and G.I. Costache. Radiation from microstrip transmission lines. In *IEEE 1988 International Symposium on Electromagnetic Compatibility*, pages 340–343, 1988.

[90] Khushboo Singh, Foez Ahmed, and Karu Esselle. Electromagnetic metasurfaces:

[91] Jinhie Skarda, Rahul Trivedi, Logan Su, Diego Ahmad-Stein, Hyounghan Kwon, Seunghoon Han, Shanhui Fan, and Jelena Vučković. Simulation of large-area metasurfaces with a distributed transition matrix method. *Conference on Lasers and Electro-Optics*, 2022.

[92] Permanand Soothar, Hao Wang, Badar Muneer, Zaheer Ahmed Dayo, and Bhawani Shankar Chowdhry. A broadband high gain tapered slot antenna for underwater communication in microwave band. *Wirel. Pers. Commun.*, 116(2):1025–1042, January 2021.

[93] Kandammathe Valiyaveedu Sreekanth, Antonio De Luca, and Giuseppe Strangi. Experimental demonstration of surface and bulk plasmon polaritons in hyper-gratings. *Scientific Reports*, 3(1), 2013.

[94] Stroud. Our focus is fresh water.

[95] Jie Sun and Kwai-Man Luk. A wideband and optically transparent water patch antenna with broadside radiation pattern. *IEEE Antennas and Wireless Propagation Letters*, 19(2):341–345, 2020.

[96] SVMicrowave. Sma female solderless litetouch pcb connector.

[97] Muhammad Tahir. Underwater wireless communication using em waves.

[98] Abitha K Thyagarajan, Priyeash Balasubramanian, Vydeki D, and Karthik M. Snr-cqi mapping for 5g downlink network. In *2021 IEEE Asia Pacific Conference on Wireless and Mobile (APWiMob)*, pages 173–177, 2021.

[99] Francesco Tonolini and Fadel Adib. Networking across boundaries: Enabling wireless communication through the water-air interface. SIGCOMM '18, page 117–131, New York, NY, USA, 2018. Association for Computing Machinery.

[100] Ming Lun Tseng, Yasaman Jahani, Aleksandrs Leitis, and Hatice Altug. Dielectric metasurfaces enabling advanced optical biosensors. *ACS Photonics*, 8(1):47–60, 2020.

[101] Dias Tulegenov and Constantinos Valagiannopoulos. Uniaxial films of maximally controllable response under visible light. *Scientific Reports*, 10(1), 2020.

[102] Rutgers University. Oblique incidence.

[103] Paul Webb. Introduction to oceanography.

[104] wirelessLANprofessionals. Mcs table and how to use it.

[105] Joseph P. S. Wong, Ariel Epstein, and George V. Eleftheriades. Reflectionless wide-angle refracting metasurfaces. *IEEE Antennas and Wireless Propagation Letters*, 15:1293–1296, 2016.

[106] Laura Wood. The worldwide underwater communication system industry is expected to reach $7.2 billion by 2030.

[107] F. Yang, B. Raeker, D. Nguyen, J. Miller, X. Ze, A. Grbic, and J. Ho. Antireflection and wavefront manipulation with cascaded metasurfaces. *Phys. Rev. Appl.*, 14:064044, Dec 2020.

[108] Songlin Yang, Yong-Hong Ye, Qinfang Shi, and Jiayu Zhang. Converting evanescent waves into propagating waves: The super-resolution mechanism in microsphere-assisted microscopy. *The Journal of Physical Chemistry C*, 124(47):25951–25956, 2020.

[109] Yuanmu Yang, Ivan I. Kravchenko, Dayrl P. Briggs, and Jason Valentine. All-dielectric metasurface analogue of electromagnetically induced transparency. *Nature Communications*, 5(1), 2014.

[110] Steve M. Young, Mark Kauf, Jeffrey Kutsch, and Anthony Grbic. Additively-manufactured all-dielectric microwave polarization converters using ceramic stereolithography. *IEEE Open Journal of Antennas and Propagation*, 4:339–348, 2023.

[111] Nanfang Yu, Patrice Genevet, Mikhail A. Kats, Francesco Aieta, Jean-Philippe Tetienne, Federico Capasso, and Zeno Gaburro. Light propagation with phase discontinuities: Generalized laws of reflection and refraction. *Science*, 334(6054):333–337, 2011.

[112] C. Zhang, Y. Xie, D. Mishra, T. Pacino, J. Shao, B. Li, J. Yuan, P. Chen, and Y. Rong. A low complexity channel emulator for underwater acoustic communications. *IEEE Transactions on Wireless Communications*, 2023.

[113] Liming Zheng and Yi Zhao. Generalized snell's law and its verification by metasurface. In Leonard Barolli, Aneta Poniszewska-Maranda, and Hyunhee Park, editors, *Innovative Mobile and Internet Services in Ubiquitous Computing*, pages 364–372, Cham, 2021. Springer International Publishing.

[114] Hong-Tao Zhou, Shao-Cong Zhang, Tong Zhu, Yu-Ze Tian, Yan-Feng Wang, and Yue-Sheng Wang. Hybrid metasurfaces for perfect transmission and customized manipulation of sound across water–air interface. *Advanced Science*, 10(19), 2023.

[115] Senlin Zhu, Emmanuel Karlo Nyarko, and Marijana Hadzima-Nyarko. Modelling daily water temperature from air temperature for the missouri river. *PeerJ*, 6, 2018.

[116] Hadzima-Nyarko M. Zhu S, Nyarko EK. Modelling daily water temperature from air temperature for the missouri river. *PeerJ*, 2018.

[117] Zygo. Stream while you swim enjoy music and more underwater.